

A unified material decomposition framework for quantitative dual- and triple-energy CT imaging

Wei Zhao^{1,2}, Don Vernekohl¹, Fei Han^{1,3}, Bin Han¹, Hao Peng¹, Yong Yang¹, Lei Xing^{1*}, James K Min^{4a)}

¹ *Stanford University, Department of Radiation Oncology, Stanford, CA 94305 USA.* ² *Department of Biomedical Engineering, Huazhong University of Science and Technology, Hubei, China.* ³ *Sun Yat-sen University Cancer Center, Department of Radiation Oncology, , Guangzhou, Guangdong, China.* and ⁴ *Dalio Institute of Cardiovascular Imaging New York-Presbyterian Hospital and Weill Cornell Medical College, New York, NY 10021 USA.*

Purpose: Many clinical applications depend critically on the accurate differentiation and classification of different types of materials in patient anatomy. This work introduces a unified framework for accurate nonlinear material decomposition and applies it, for the first time, in the concept of triple-energy CT (TECT) for enhanced material differentiation and classification as well as dual-energy CT.

Methods: We express polychromatic projection into a linear combination of line integrals of material-selective images. The material decomposition is then turned into a problem of minimizing the least-squares difference between measured and estimated CT projections. The optimization problem is solved iteratively by updating the line integrals. The proposed technique is evaluated by using several numerical phantom measurements under different scanning protocols. The triple-energy data acquisition is implemented at the scales of micro-CT and clinical CT imaging with commercial "TwinBeam" dual-source DECT configuration and a fast kV switching DECT configuration. Material decomposition and quantitative comparison with a photon counting detector and with the presence of a bow-tie filter are also performed.

Results: The proposed method provides quantitative material- and energy-selective images examining realistic configurations for both dual- and triple-energy CT measurements. Compared to the polychromatic kV CT images, virtual monochromatic images show superior image quality. For the mouse phantom, quantitative measurements show that the differences between gadodiamide and iodine concentrations obtained using TECT and idealized pho-

ton counting CT (PCCT) are smaller than 8 mg/mL and 1 mg/mL, respectively. TECT outperforms DECT for multi-contrast CT imaging and is robust with respect to spectrum estimation. For the thorax phantom, the differences between the concentrations of the contrast map and the corresponding true reference values are smaller than 7 mg/mL for all of the realistic configurations.

Conclusions: A unified framework for both dual- and triple-energy CT imaging has been established for the accurate extraction of material compositions using currently available commercial DECT configurations. The novel technique is promising to provide an urgently needed solution for several CT-based diagnostic and therapy applications, especially for the diagnosis of cardiovascular and abdominal diseases where multi-contrast imaging is involved.

I. INTRODUCTION

In computed tomography (CT) imaging, the CT number corresponds to the effective linear attenuation coefficient of a voxel and its value depends on the X-ray photon energy. In reality, it is possible that two voxels of the same material have different CT numbers (or effective linear attenuation coefficients), as the effective energy may be location dependent due to the beam hardening effect. Furthermore, the CT number of a voxel depends on both the atomic number and the mass density of the material, making material decomposition from a single-energy CT impossible without additional information. To circumvent the problem, dual-energy CT (DECT) has been developed to allow for material discrimination, by adding another attenuation measurement with a different energy spectrum^{1,2}. DECT has been a valuable tool in a range of emerging clinical applications, including automated bone removal in angiography, blood volume measurement in perfusion CT, urinary stone characterization and gout diagnosis³. Practically, dual-energy attenuation measurements have been implemented in different ways, including the fast switching of X-ray tube potentials in a single scan^{4,5}, dual X-ray sources on the same gantry², and layered detectors⁶. The measured dual-energy projection data sets are then employed to yield energy- and material-selective images using dual-energy material decomposition methods. Depending on the data acquisition technique, dual-energy material decomposition can be performed in projection domain, image domain, or projection- and image- domain jointly.

Like many other material decomposition methods⁷⁻¹⁶, the linear attenuation coefficient is expressed as a linear combination of two basis materials in projection domain methods. Thus, the polychromatic high- and low-energy

projections become functions of the line integrals of the basis material images. This reduces the problem of material decomposition to the determination of the integrals of these basis material images using the high- and low-energy projections and a decomposition function. The decomposition function can be approximated by, for example, a polynomial where its coefficients are determined by calibrations with dedicated experimental phantoms¹⁰. Basis material sinograms obtained using the decomposition functions are then employed to reconstruct the basis material images using standard image reconstruction algorithms. Alternatively, dual-energy material decomposition can be implemented in image-domain^{17,18}. Here, high- and low-energy CT images are first reconstructed using the corresponding raw projections and material decomposition is then performed in image domain by linearly combining the CT images. As the acquired high- and low-energy CT data are usually geometrically inconsistent in practice (i.e., the paths of the two measurements are different, even for the fast kVp switching technology), the material decomposition in image-domain is more convenient. Like projection-domain methods, a series of calibration measurements for the basis materials in high- and low-energy are also required. However, material-selective images generated this way are basically a linear combination of the high- and low-energy CT images. Compared to nonlinear projection domain methods, this leads to reduced contrast-to-noise ratio and residual artifacts in the decomposed images¹⁹.

Dual-energy material decomposition in the third way generates the material images directly from dual-energy attenuation measurements with incorporation of a projection matrix²⁰⁻²³. In this case, material decomposition is formulated as an optimization problem, and statistical models and regularization are often introduced into the objective function to reduce noise and improve image quality. Material decomposition in this approach is usually computationally expensive because of repeated forward and backward projections as well as complicated optimization procedures, which may be undesirable for clinical applications.

Although DECT material decomposition yields images with significantly reduced beam hardening artifacts and allows a quantitative characterization of two different materials (e.g., contrast medium and calcified tissues)²⁴, there are many applications in which the discrimination of more than two materials is needed. Indeed, the human body contains different materials, such as blood, water, bone, and often endogenous contrast agent during imaging. Thus a material decomposition method capable of discriminating more than two materials is highly desirable. In general, the problem of obtaining more than two material-specific images can be solved either in image-domain²⁵⁻²⁷ or with energy-resolving photon counting detectors²⁸⁻³². The former approach, however, is not as accurate as projection-domain methods because of residual beam hardening artifacts. The use of photon-counting detectors is still at an early stage and there are a number of technical issues, such as charge sharing³³ and pulse pileup, yielding to distorted

spectrum information, which have yet to be resolved. While it is possible to use more than two energy measurements for multi-material decomposition^{34,35}, currently, only methods in image-domain exist to accomplish the task. The purpose of this work is to establish a unified nonlinear projection-domain framework for both dual- and triple-energy material decomposition.

II. METHODS

II.A. Principle of basis material decomposition

For diagnostic X-ray imaging, the attenuation properties of materials can be modeled using the two dominant physical interactions, i.e., photoelectric and Compton. Based on this assumption, in the theory of material decomposition, the linear attenuation coefficient $\mu(\vec{r}, E)$ of a material is assumed to be modeled as a linear combination of two basis functions,

$$\mu(\vec{r}, E) = f_1(\vec{r})\psi_1(E) + f_2(\vec{r})\psi_2(E), \quad (1)$$

here \vec{r} represents the three-dimensional spatial coordinates of a specific pixel and E is the photon energy. Basis functions $\psi_{1,2}$ are the independent energy dependencies which can be mass attenuation coefficients of known materials (i.e., basis materials) and $f_{1,2}(\vec{r})$ are material-specific images (specific to the basis materials). However, if an element has a K-edge in the diagnostic energy range (for example, gadolinium), then the attenuation coefficient of the material cannot be decomposed solely with two basis materials when bone is also present. This is because the specific K-edge can not be characterized by either Compton or photoelectric which are the dominant absorption mechanisms in the diagnostic energy range. Hence, the decomposition in (1) has to be extended to include a third term, which can characterize the attenuation properties of the element. In this case, the decomposition of the material becomes,

$$\begin{aligned} \mu(\vec{r}, E) &= f_1(\vec{r})\psi_1(E) + f_2(\vec{r})\psi_2(E) + f_3(\vec{r})\psi_3(E) \\ &= \sum_{i=1}^3 f_i(\vec{r})\psi_i(E) \end{aligned} \quad (2)$$

where $\psi_i(E)$ with $i = 1, 2, 3$ are the known mass attenuation coefficients of the basis materials, including the K-edge material, and $f_i(\vec{r})$ are the location-dependent material-specific images. Without extra conditions, the extended formulation (2) implies the need of a third attenuation measurements to obtain material-specific information.

II.B. Material images-based polychromatic reprojection

Based on the material decomposition formulation (1) and (2), the polychromatic X-ray transmission measurement of the material can be estimated as

$$\hat{p} = -\log \int_0^{E_{max}} dE \Omega(E) \eta(E) \exp \left[-\sum_{i=1}^N \psi_i(E) A_i \right], \quad (3)$$

with $N = 2$ for two material case and $N = 3$ for three material case, and with $A_i = \int d\vec{r} f_i(\vec{r})$ the line integrals of the material-selective images (i.e. material density images). $\Omega(E)$ is the corresponding polychromatic energy spectrum of the ray and the integral in (3) goes over the energy range of the spectrum. $\eta(E)$ is the energy dependent detection efficiency. Note that \hat{p} depends on the detector pixel and the pixel channel index is dropped for convenience.

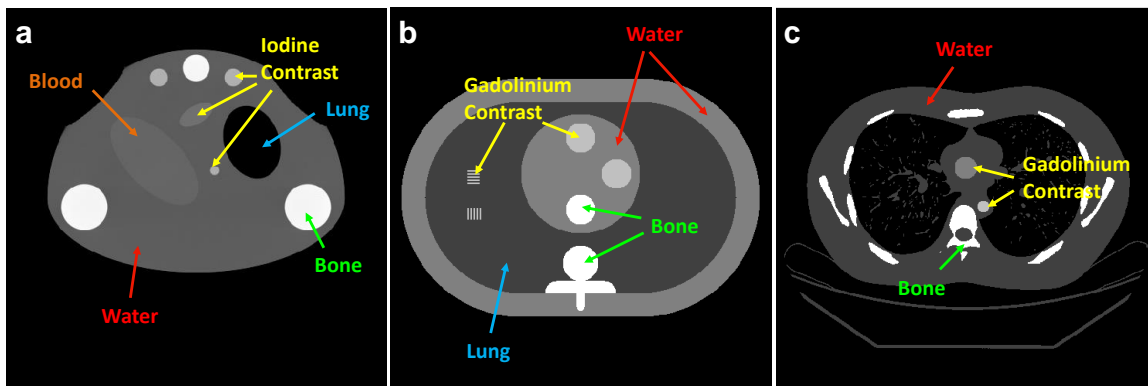


FIG. 1 Imaging phantoms used in the numerical studies. (a) Modified micro-CT mouse phantom with blood, lung, bone and contrast agents inserts. The iodine contrast agents have two concentrations, 5 mg/mL and 10 mg/mL. (b) Modified thorax phantom showing two coronary arteries in the heart region and two bar patterns in the lung region both filled with gadolinium contrast agents. (c) Anthropomorphic thorax modified from clinical CT image showing contrast agents in the heart region.

II.C. Material decomposition

As mentioned above, to enable a three material decomposition, i.e., calculate the line integrals of the three material-specific images, one has to perform three transmission measurements using different energies, otherwise the system is underdetermined. Meanwhile, based on the polychromatic reprojection (3), for each detector channel, the reprojected value \hat{p} should equal to the corresponding raw measurement p_m . However, in realistic application, the acquired energy spectrum $\Omega(E)$ is prone to suffer from error, additionally, the residual scatter radiation as well as the projection noise (quantum noise and electronic noise) cause inconsistency between the measured data and the data calculated using reprojection model. Hence, instead of directly solving the line integrals of the material-specific images from (3), we minimize the quadratic error between the measured data p_m and the estimated projection \hat{p} with respect to the line

integrals A_i , i.e.,

$$A_i^* = \arg \min_{A_i \geq 0} \|\mathbf{p}_m - \hat{\mathbf{p}}(A_i)\|_2^2. \quad (4)$$

Here $i = 1, 2$ for dual-energy case, and $i = 1, 2, 3$ for triple-energy case. The vector \mathbf{p}_m denotes the dual- or triple-energy transmission measurements for each detector pixel, i.e., $\mathbf{p}_m = (p_m^H, p_m^L)$ or $\mathbf{p}_m = (p_m^H, p_m^M, p_m^L)$, where p_m^H , p_m^M , and p_m^L are the high-, median-, and low-energy measurements, respectively. $\hat{\mathbf{p}}$ is the corresponding estimated projection using line integrals of the density images. Since A_i is the line integral of the density image, we have non-negative constraint on A_i . The optimization problem (4) can be solved in a pixel-wise fashion using a multi-variable downhill simplex method (Nelder-Mead method). Implementation details and pseudo code of the method can be found in VII. Once A_i was determined for all of the pixels, material-specific density images can be reconstructed by using the standard filtered backprojection algorithm.

III. SIMULATION STUDIES

In order to evaluate the proposed method, we performed simulation studies using various phantoms in scale of both clinical CT and micro-CT applications.

III.A. Numerical phantoms description

We simulated three test phantoms to show the performance of the nonlinear material decomposition method. The first mouse phantom which is in scale of micro-CT application and modified from the phantom as defined by Stenner and Kachelriess in¹⁰, consists of inserts that contain different iodine concentrations. Compared to the original phantom in¹⁰, we have replaced the low contrast and the bone inserts with blood and standard cortical bone inserts, respectively. Concentrations for the two iodine contrast agent inserts are 5 and 10 mg/mL.

The second phantom is a simplified thorax phantom and is in scale of clinical diagnostic CT application. It contains two coronary arteries filled with contrast agent in the heart region. In order to depict the preservation of spatial resolution, two contrast agent bar patterns are also included in the lung region. Compared to the second one, the third anthropomorphic thorax phantom is more realistic as it was generated using clinical CT images. To

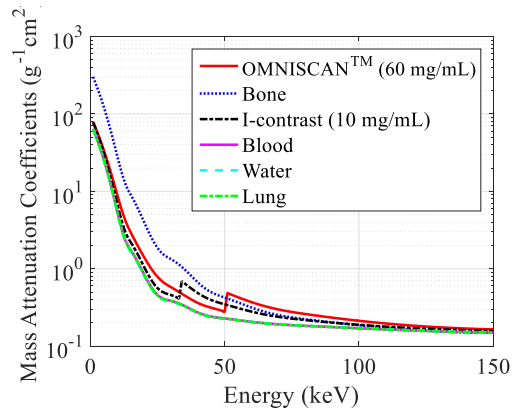


FIG. 2 Mass attenuation coefficients of the materials in this study. Note that although blood, water, and lung have similar mass attenuation coefficients, their linear attenuation coefficients are different due to their different mass density.

perform triple-energy material decomposition, we have added two contrast agent inserts in the heart region. Since both of the thorax phantoms are scanned using clinical CT protocols which have relatively high kV settings and thick inherent filtrations, we have used gadolinium (Gd) as contrast agent for both thorax phantoms as the K-edge energy for gadolinium is 50.2 keV while it is 33.2 keV for iodine. Specifically, we model OMNISCANTM as the contrast agent which contains 287 mg/mL gadodiamide and with a mass density of 1.15 g/cm³. The gadodiamide has the stoichiometric formula of C₁₆H₂₈GdN₅O₉. To be more realistic, concentration of gadodiamide of the OMNISCANTM is diluted to 60 mg/mL. The phantoms used in this study are shown in Fig. 1.

During the simulation, all of the mass attenuation coefficients are obtained or calculated from the NIST database. For the materials which can not be found in the database, such as the contrast agents, their mass attenuation coefficients are calculated using their chemical elements and the corresponding mass fractions. Figure 2 shows the mass attenuation coefficients of the materials used in the simulation studies. Note that the y axis is plotted on a logarithmic scale. One can observe the K-edge energies of the iodine and gadolinium contrast agents. Properties of the materials used in this study are summarized in Table I.

TABLE I Properties of the materials used in the numerical simulation studies. Note that we have diluted the OMNISCANTM to 60 mg/mL and its density is reduced from 1.15 g/cm³ to 1.03 g/cm³.

| Material name | Density (g/cm ³) |
|---|------------------------------|
| Water | 1.000 |
| Lung | 0.260 |
| Bone | 1.850 |
| Blood | 1.060 |
| Iodine contrast agent (5 mg/mL, 10 mg/mL) | 1.004, 1.008 |
| OMNISCAN TM (60 mg/mL) | 1.031 |

III.B. Energy spectra

For the micro-CT mouse phantom study, we use 40 kV, 60 kV and 80 kV spectra for the triple-energy transmission measurements. These three spectra are generated using the most recent spectrum generator, Spektr 3.0³⁶, with 0 mm Al, 5 mm Al, and 0.3 mm Cu filtrations, respectively. In addition, all of the three sources have 2 mm Al inherent filters. We use the low 40 kV and the high 80 kV spectra for dual-energy measurements and all the three spectra for triple-energy CT measurements. In order to accurately calculate \hat{p} , the energy spectrum used in (3) should be modeled precisely. There are a lot of methods that can be employed to obtain the spectrum³⁷⁻⁴¹. In this study, we employ an indirect transmission measurement (ITM) method to estimate the triple energy spectra³⁷. Specifically, the energy spectrum is expressed by a set of model spectra. By updating each weight of the model spectra, the spectrum estimation method minimizes the difference between the ITM and the projection of a uniform water phantom. The final spectrum is calculated using the model spectra and their weights. The estimated spectra are then employed for the triple-energy material decomposition. To further evaluate the robustness of the proposed material decomposition method over spectrum estimation accuracy, triple-energy material decomposition is performed using spectra estimated with two sets of different model spectra.

For the triple-energy thorax phantoms studies, it is natural to take advantage of the current commercial dual-energy CT (DECT) configurations to acquire triple-energy CT data sets as DECT scanners are widely used in clinical applications nowadays. This is beneficial over sequentially scanning the subject with three different energies or using three source-detector sets on the same gantry. For the dual-source DECT scanner, one can use a "TwinBeam" configuration on one of the X-ray sources³⁵ to enable the simultaneous acquisition of a triple-energy measurement. With the "TwinBeam" configuration, X-ray photons emitted from the source tube are prefiltered before arriving at the subject by two different filters, and each filtered spectrum covers half of the detector rows.

To reduce noise during material decomposition, one would expect the filtered spectra should be quite different from each other such that the difference between their transmission measurements of the sample is as large as possible. To this end, it is better to choose K-edge filters to separate the spectra. Because K-edge filters significantly attenuate X-ray photons whose energy are higher than the K-edge energy. This feature can be exploited to generate high- and low-energy spectra, where the high-energy spectrum is generated by the filter with low K-edge energy and the low-energy spectrum is generated by the filter with high K-edge energy. For example, as shown in³⁵, for a 150 kV incident spectrum, tin (Sn) filter is employed to generate a hardened spectrum, while gold (Au) and bismuth (Bi) filter set is used to soften the spectrum.

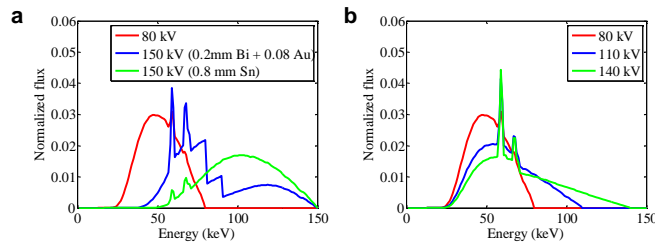


FIG. 3 Energy spectra used in the numerical simulation studies of clinical diagnostic CT applications. (a) Siemens scenario, Bi and Au filters are used to filter high energy photons to yield a median energy spectrum, while Sn filter is used to filter low energy photons to yield a high energy spectrum. (b) GE scenario, fast kV switching spectra with the same filtration.

In this study, to evaluate the proposed method, we performed material decomposition using two different sets of spectra, "TwinBeam" dual-source spectra and fast kV switching spectra, i.e., Siemens scenario and GE scenario. For the Siemens scenario, a 0.6 mm Sn was used to filter a 150 kV spectrum to yield high-energy spectrum and 0.08 mm Au + 0.1 mm Bi recombination filters were used to yield median-energy spectrum. These two spectra together with a 70 kV spectrum make up the triple-energy CT configuration. For the GE scenario, instead of fast switching between high kV and low kV, the scanner performs an additional median kV measurement for triple-energy CT. Since it is technically difficult to change filtration during CT scan in this configuration, all of the triple-energy measurements use the same filtration. Figure 3 depicts the spectra used for the simulation studies. For the "TwinBeam" dual-source DECT configuration (Fig. 3 (a)), one can achieve triple-energy measurement using different kVs as well as different filtrations. Since the K-edge energies for bismuth (Bi) and gold (Au) are 80.7 and 90.5 keV, respectively, the bismuth and gold filters are used to filter high energy photons to yield a median-energy spectrum for the triple-energy measurement. To the contrary, tin filter whose K-edge energy is 29.2 keV, is used to filter low-energy photons and yield high-energy spectrum. For the fast kV switching configuration (Fig. 3 (b)), the triple-energy measurements are performed using different kVs but the same filtration.

To be more realistic, the proposed method was also tested on the anthropomorphic thorax phantom including a bow-tie filter in the acquisition geometry. In this case, the Siemens DECT configuration was used with the bow-tie filter attached behind the K-edge filters, i.e., between the K-edge filters and the phantom. Figure 4(a) shows one source-detector set for this configuration. Figure 4(b) shows the normalized photon intensity of the detector without the presence of the phantom. All the used spectra for the thorax phantoms studies are generated using Spektr 3.0³⁶.

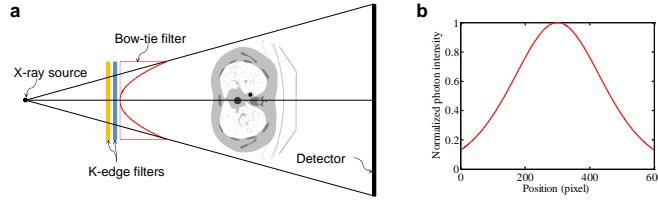


FIG. 4 Anthropomorphic thorax phantom study using bow-tie filter. (a) CT scan geometry with the bow-tie filter and K-edge filters. (b) Flood field of the bow-tie filter.

III.C. Projection data acquisition

All of the simulations were performed using 2D fan-beam geometry with an ideal point X-ray source. The linear detector array consists of 1024 pixels and each pixel is $0.388 \text{ mm} \times 0.388 \text{ mm}$. Since one difficulty of material decomposition is ill-conditioning, which yields material images with increased noise, Poisson noise is included in the simulations to validate the robustness of the projection domain material decomposition method. The fan beam CT projection data sets were simulated by polychromatic forward projecting the micro-CT phantom and the thorax phantoms. Mathematically, the projection data can be represented as:

$$I = \int_0^{E_{max}} dE \eta(E) \text{Poisson} \left\{ N \Omega(E) \exp \left[- \int \mu(\vec{r}, E) d\vec{r} \right] \right\}, \quad (5)$$

with N the total number of incident photons and it was set to the order of 10^6 for all of the clinical CT studies. To be realistic, we simulated an energy-integrating detector, thus the energy dependent response $\eta(E)$ was considered to be proportional to photon energy E . E_{max} is the maximum energy of the polychromatic spectrum $\Omega(E)$. In the energy integrating mode, all the photons arriving on a specific detector pixel for a single view angle are summed up according to their energies. The energy-dependent linear attenuation coefficient $\mu(\vec{r}, E)$ was obtained from the National Institute of Standards and Technology (NIST) database. During the simulations, the propagation path length for each ray in each material is calculated using either an analytical method or a numerical ray-tracing method. To generate a Poisson distributed photon count, we first calculate the mean photon number $N'(E) = N \Omega(E) \exp \left[- \int \mu(\vec{r}, E) d\vec{r} \right]$ that arrive at the detector for each energy bin. A random number is then generated from the Poisson distribution with $N'(E)$ as the mean parameter^{42–44}. These random photon numbers are weighted by their energies (energy integration) and detection efficiencies and finally summed up.

For the simple micro-CT mouse phantom, note that it consists of ellipses and circles which have explicit mathematical forms, we can use the analytical method. In this case, the propagation path length for each pixel in each ellipse

or circle is the intersection length of the line (i.e., the ray connecting the pixel and X-ray source) and the specific ellipse or circle. Thus it can be analytically solved using the geometry equations of the line, ellipse and circle. For the complicated thorax phantoms, we have to use the numerical method. In this case, the intersection length of the ray and each voxel (with size of 0.45 mm) is numerically calculated and added up for the same material to yield the corresponding propagation path length. Due to its computation load and parallel feature, this method is implemented on a graphics processing unit (GPU)⁴⁵ for considerable acceleration.

III.D. Comparison studies

Simultaneous multi-contrast CT imaging is very useful for the diagnosis of cardiovascular and abdominal diseases. The relevant clinical applications include characterization of atherosclerotic plaque composition⁴⁶, colonography⁴⁷, and so on. In this case, DECT cannot provide accurate contrast images, while triple-energy CT (TECT) can provide quantitative multi-contrast images. In order to show the merit of TECT, a modified mouse phantom where the blood insert is replaced by gadolinium contrast and the bone inserts are replaced by air, is investigated using both DECT and TECT. In addition, comparison study with a widely used sinogram domain method, EDEC method¹⁰, is also included. The EDEC method is an empirical nonlinear algorithm based on calibration measurements using basis materials. In this study, we have employed a two-cylinder phantom for calibration.

Photon counting detector-based CT imaging is getting more and more attention from clinical side recently^{48,49}. It has several superior features where quantitative imaging and direct tissue characterization are the most important features in clinical applications. To further evaluate the performance of the proposed method, the method is compared to a nonlinear method based on photon counting detectors²⁸. The latter method models the projection counting data as Poisson signals and formulates the material decomposition process as a maximum-likelihood optimization problem.

IV. RESULTS

We first show the results of dual-energy material decomposition and comparison study with idealized photon counting CT (PCCT) using the micro-CT mouse phantom, and then we present the TECT results using simplified and anthropomorphic thorax phantoms in the scale of clinical applications. Result with the application of bow-tie filter is also presented.

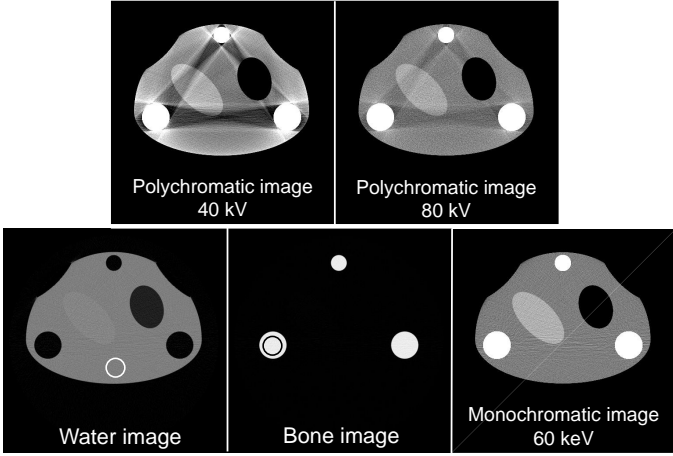


FIG. 5 Dual-energy CT images of the micro-CT mouse phantom without contrast agent at 40 kV/80 kV, and material-selective images obtained using the proposed method. The beam-hardening artifacts free monochromatic image is a linear combination of the basis material images. Display window for the CT images and monochromatic image: $[-200, 200]$ HU, and for the material images $[0, 2]$ g/cm^3 .

IV.A. Dual-energy material decomposition

Figure 5 shows the results of dual-energy material decomposition using the mouse phantom. The first row depicts polychromatic 40 kV and 80 kV CT images. It is visible that there are severe beam hardening artifacts in the CT images, especially in the 40 kV image. This is because for the 40 kV spectrum, the linear attenuation coefficients of the materials undergo a larger change, compared to 80 kV spectrum. The second row shows the basis material images and the monochromatic image at 60 keV. The monochromatic image is the weighted summation of the basis material images with the weights from linear attenuation coefficients of basis materials at 60 keV. Quantitative measurements of the decomposed material images match the true densities of blood and bone quite well. Compared to the standard polychromatic CT images, beam hardening artifacts are completely removed in the composed virtual 60 keV image. Note that the CT images and the monochromatic image are normalized to Hounsfield units (HU) with value measured in the central water region and with the linear attenuation coefficient of water at 60 keV, respectively.

IV.B. Triple-energy material decomposition

The results of TECT imaging using the micro-CT mouse phantom are shown in Fig. 6. For comparison, we also present the results of the phantom using idealized photon-counting detector. Figure 6 (a) and (b) show the spectra of ideally separated photon counting bins for PCCT and spectra for the triple-energy measurements, respectively. Different from dual-energy case, we have added a third 60 kV measurement between the low- and high-kV energy measurements. Figure 6(c-e) depict the reconstructed polychromatic CT images using triple-energy measurements.

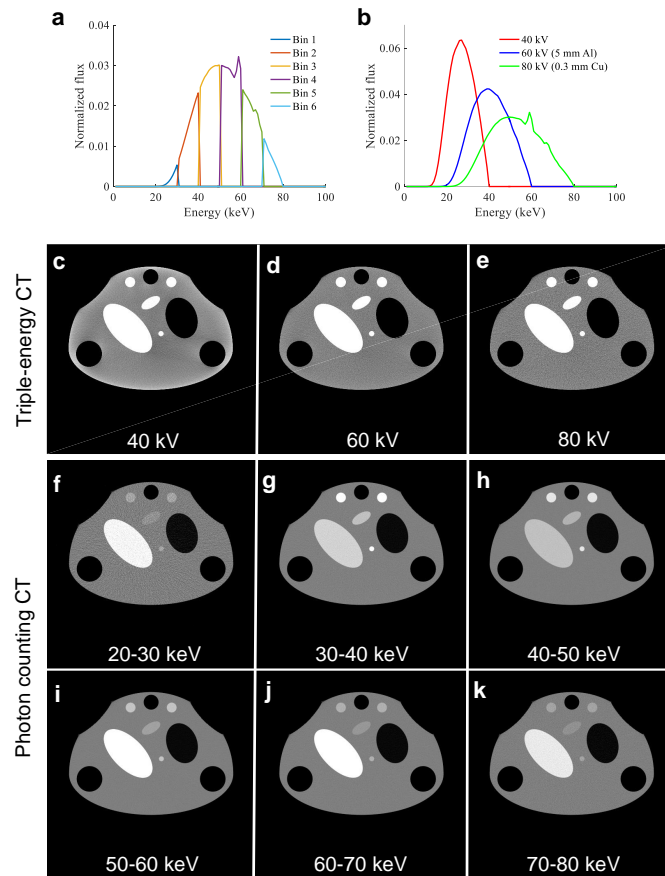


FIG. 6 Results of CT images of the multi-contrast micro-CT mouse phantom using both idealized PCCT and TECT. (a) Energy spectra for ideally separated photon counting bins of the PCCT, (b) energy spectra used for triple-energy measurements. (c)-(e) Polychromatic CT images reconstructed using projection acquired with TECT, and (f)-(k) images reconstructed using each energy bin of PCCT. All CT images are normalized to Hounsfield units and windowed to ($C=0$ HU/ $W=400$ HU).

Beam hardening artifacts are introduced in the 40 kV images, especially at the peripheral region of the phantom. The artifacts are reduced as the energy of the spectrum increases, as expected. Figure 6(f-k) depict the images reconstructed using projection acquired with the six energy bins of the photon counting detector. From energy bin 20-30 keV to 30-40 keV, we can see the attenuation of iodine contrast agent increases strongly, indicating the K-edge property of the iodine, which is at 33.2 keV. From energy bin 40-50 keV to 50-60 keV, the blood insert which is replaced by the gadolinium contrast increases strongly. This is because the K-edge of gadolinium is at 50.2 keV. Note that all images were normalized to Hounsfield units with respect to the value measured in the central water region.

Figure 7 shows triple-energy spectra estimated using a uniform water cylinder with two sets of model spectra. The first, second and third rows show spectra estimation for 40, 60 and 80 kV, respectively. Figure 7(c, h, m) are spectra estimated using model spectra Fig. 7(b, g, l). As can be seen, the estimated spectra match with the reference spectra quite well. Figure 7(e, j, o) are spectra estimated using model spectra Fig. 7(d, i, n). In this case, the model spectra do not contain the reference spectrum, which is much more difficult to accurately recover the reference spectra. Hence,

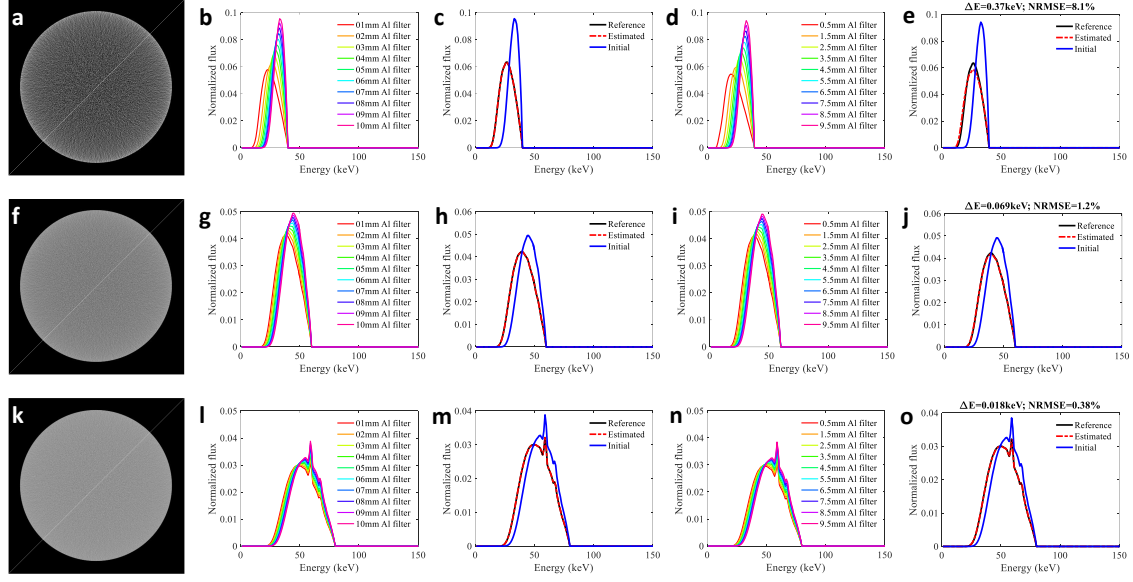


FIG. 7 Energy spectra estimation using a water phantom with different model spectra. The first, second and third rows show spectra estimation for 40, 60, and 80 kV, respectively. (c, h, m) are spectra estimated using model spectra (b, g, l), respectively. (e, j, o) are spectra estimated using model spectra (d, i, n), respectively.

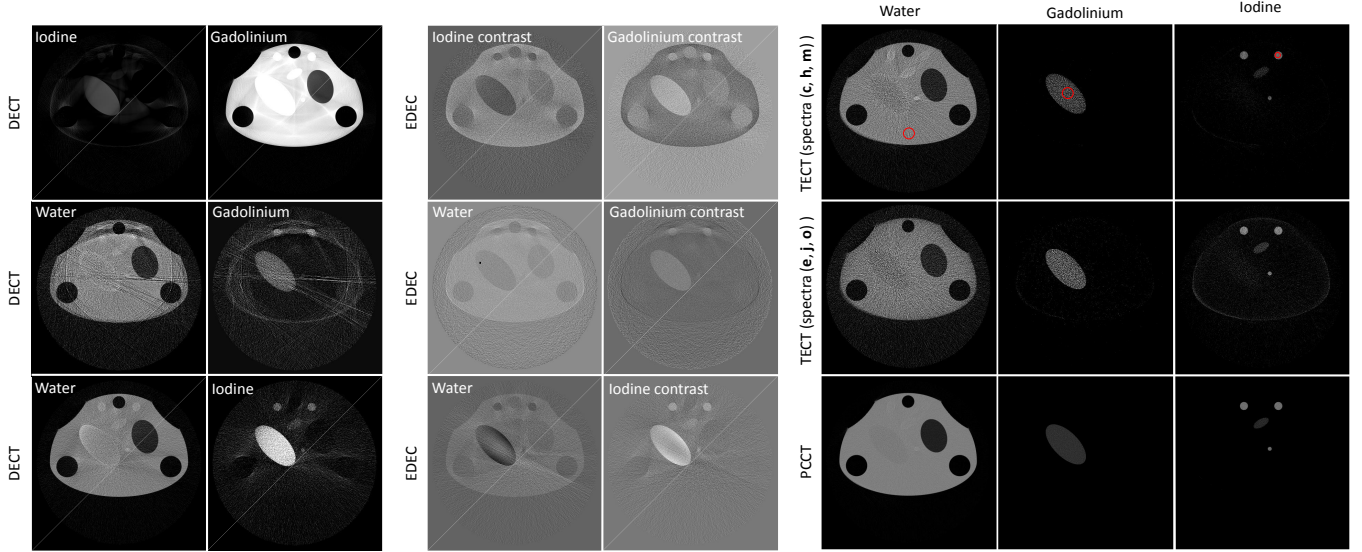


FIG. 8 Results of multi-contrast material decomposition using DECT, EDEC, TECT and idealized PCCT data. DECT and EDEC cannot obtain reasonable material-specific images, while both TECT and PCCT can provide accurate material-specific images. For DECT, TECT and PCCT, Water, gadolinium and iodine images are windowed to $[0, 2]$, $[0.05, 0.15]$, and $[0.002, 0.02]$ g/cm³, respectively.

the estimated spectra in Fig. 7(e, j, o) are not as accurate as spectra in Fig. 7(c, h, m). Mean energy differences ΔE between the estimated spectra and reference spectra are 0.37, 0.07 and 0.02 keV for the 40, 60 and 80 kV spectra, respectively. Normalized root mean square errors between the estimated spectra and the reference spectra are 8.1%, 1.2%, and 0.4%, respectively.

Figure 8 shows the results of material decomposition using DECT, TECT and idealized PCCT data. As can be seen, for DECT and EDEC material decomposition, no matter how to choose the basis materials (iodine/gadolinium,

TABLE II Quantitative measurements of the material-specific images of the mouse phantom decomposed using DECT, TECT and PCCT. TECT¹, TECT² correspond triple-energy material decomposition using spectra show in Fig. 7(c, h, m) and (e, j, o), respectively.

| Density and concentration | | Measured | Difference |
|----------------------------|-------------------|----------|------------|
| Water (g/cm ³) | DECT | 1.00 | 0 |
| | TECT ¹ | 0.98 | -0.02 |
| | TECT ² | 0.89 | -0.11 |
| | PCCT | 1.00 | 0 |
| Gadodiamide (mg/mL) | DECT | - | - |
| | TECT ¹ | 63 | 3 |
| | TECT ² | 68 | 8 |
| | PCCT | 60 | 0 |
| Iodine (mg/mL) | DECT | - | - |
| | TECT ¹ | 9 | -1 |
| | TECT ² | 11 | 1 |
| | PCCT | 10 | 0 |

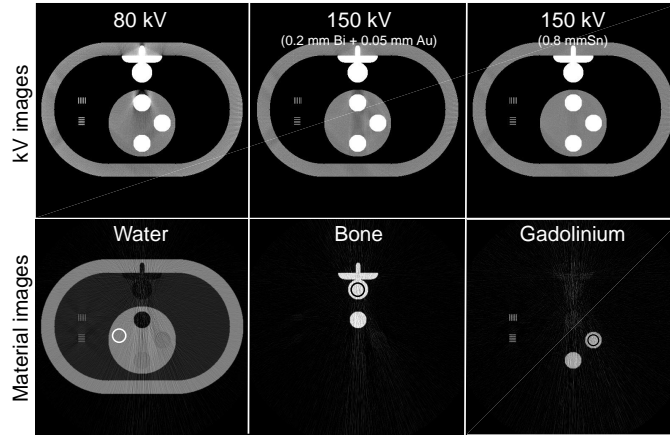


FIG. 9 Results of the simplified thorax phantom using triple-energy CT with TwinBeam Dual-source configuration. The labeled circles are used for quantitative measurements. The decomposed densities match with the true densities quite well. All of the kV images are windowed to $[-200, 200]$ HU. Water and bone images are windowed to $[0, 2]$ g/cm³, and gadolinium images are windowed to $[0, 0.1]$ g/cm³.

water/gadolinium and water/iodine), one cannot obtain reasonable material-specific images. For TECT and PCCT material decomposition, water, gadodiamide and pure iodine are selected as the basis materials. Both methods can provide superior material-selective images. In addition, TECT material decomposition using spectra estimated with different model spectra show comparable image quality, suggesting the method is robust with respect to spectrum estimation. Quantitative measurements indicate TECT decomposed densities of the materials are comparable with that obtained by PCCT, as shown in Table II.

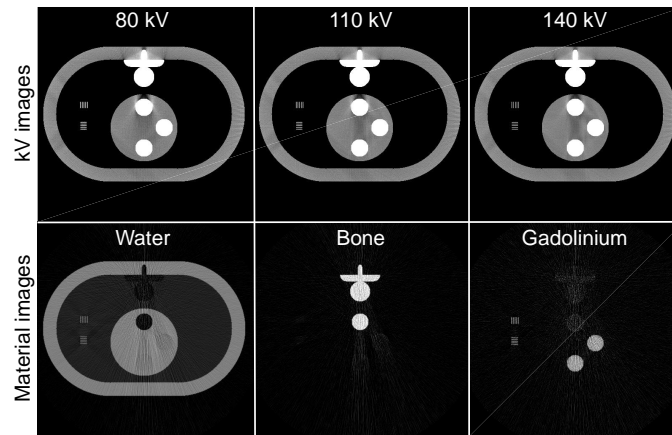


FIG. 10 Results of the simplified thorax phantom using triple-energy CT with fast kV switching configuration. The labeled circles are used for quantitative measurements. The decomposed densities match with the true densities quite well. All of the kV images are windowed to $[-200, 200]$ HU. Water and bone images are windowed to $[0, 2]$ g/cm³, and gadolinium images are windowed to $[0, 0.1]$ g/cm³.

IV.C. TwinBeam Dual-source configuration

Figure 9 shows the results of material decomposition images using triple-energy measurements with "TwinBeam" dual-source configuration. The first row from left to right shows the polychromatic CT images at 80 kV, 150 kV with 0.2 mm bismuth plus 0.05 mm gold filter and 150 kV with 0.5 mm tin filter, respectively. Beam hardening artifacts in the CT images are reduced gradually as the mean energies of the spectra increase. The second row depicts the decomposed images with water, bone, and gadodiamide as basis materials. It is visible that gadodiamide is well decomposed from the contrast agent solution. Quantitative measurements are shown in Table III.

IV.D. Fast kV switching configuration

The results of the simplified thorax phantom using triple-energy CT with fast kV switching configuration are shown in Fig. 10. The first row depicts the polychromatic CT images at 80, 110, and 140 kV. As can be seen, the beam hardening artifacts are present in all of the kV images and do not reduce as the energy increase. This is because the filtration can not be changed in this configuration; resulting in a broad spectrum for the high kV setting. The second row shows the decomposed images with water, bone, and gadodiamide as the basis materials. Gadodiamide is well decomposed from the contrast agent. Quantitative measurements show the decomposed densities match with the true densities quite well (Table III).

TABLE III Quantitative measurements of the material-specific images of the simplified thorax phantom and the anthropomorphic thorax phantom decomposed using TECT with TwinBeam dual-source (TB-DS), fast kV switching (fKV), and TwinBeam dual-source at the presence of a bow-tie filter (TB-DS-BT).

| Density and concentration | | Measured | Difference |
|----------------------------|----------|----------|------------|
| Water (g/cm ³) | TB-DS | 1.006 | 0.006 |
| | fKV | 1.007 | 0.007 |
| | TB-DS-BT | 1.035 | 0.035 |
| Bone (g/cm ³) | TB-DS | 1.727 | -0.123 |
| | fKV | 1.724 | -0.126 |
| | TB-DS-BT | 1.641 | -0.209 |
| Contrast (mg/mL) | TB-DS | 56 | -4 |
| | fKV | 53 | -7 |
| | TB-DS-BT | 55 | -5 |

IV.E. Anthropomorphic thorax phantom with bow-tie filter

Figure 11 shows the results of the anthropomorphic thorax phantom using "TwinBeam" dual-source triple-energy configuration at the presence of bow-tie filter. The first row shows the kV images and we can see marginal beam hardening artifacts in all of the images. In addition, the attenuation coefficients (HU value) at the peripheral of the thorax phantom are lower than the other regions which differs from the behavior of the simplified thorax phantom images. This can be attributed to the application of the bow-tie filter, with which the spectrum at the peripheral region is harder than in the central region, resulting in a smaller attenuation contribution in the reconstructed CT images.

The decomposed images in the second row suggest gadodiamide is well separated from the soft tissue and bone. Quantitative measurements show that the decomposed densities are close to the true densities of the basis materials (Table III).

V. DISCUSSION

Based on currently available dual-source and fast kV switching DECT configurations, we provide a unified framework to perform triple-energy material decomposition, and demonstrated its feasibility using realistic applications with estimated spectra. Multi-contrast imaging shows the benefit of TECT over DECT. DECT and EDEC need a third energy measurement or calibration to provide accurate multi-contrast images. Material images generated by the proposed method are comparable to those generated with the idealized photon-counting detector. With the limitations of current energy-resolved photon-counting detector, the proposed method represents a major step toward realistic

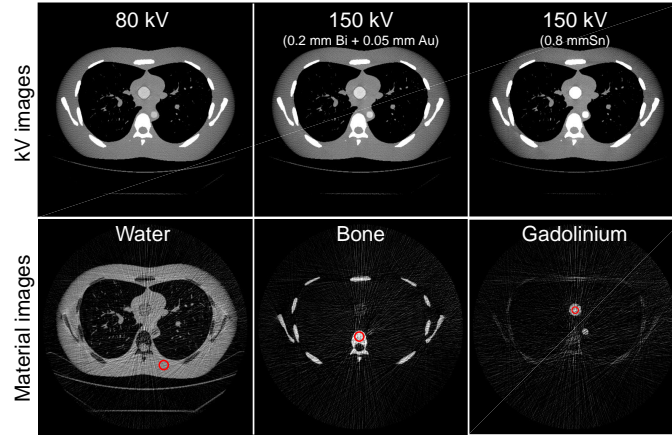


FIG. 11 Results of the anthropomorphic thorax phantom using triple-energy CT with TwinBeam Dual-source configuration at the presence of a bow-tie filter. The labeled circles are used for quantitative measurements. The decomposed densities match with the true densities quite well. All of the kV images are windowed to $[-500, 500]$ HU. Water and bone images are windowed to $[0, 2]$ g/cm^3 , and gadolinium images are windowed to $[0, 0.1]$ g/cm^3 .

TECT imaging and is potential useful for clinical applications.

Based on (3) and (4), in order to perform material decomposition as accurate as possible, one has to accurately model the energy spectrum $\Omega(E)$. There are several different ways to obtain the spectrum $\Omega(E)$. The first way is to directly measure the spectrum using energy-resolved photon-counting detectors (such as cadmium zinc telluride and cadmium telluride detectors). However, the accuracy of direct measurement usually suffers from spectral distortion which is caused by charge sharing, pulse pileup, and K-escape energy loss. Hence, it is desirable to model³³ or correct⁵⁰ the spectrum distortion before material decomposition. Alternatively, one can use direct or indirect transmission³⁷ measurements to obtain an effective energy spectrum which incorporates the contribution of inherent filtration and detector response functions.

In realistic raw projection data sets, the acquisition with the "TwinBeam" dual-source configuration is inconsistent, which means that the obtained dual- and triple-energy measurements are not from the same X-ray path. However, the proposed method is performed in projection domain which requires consistent raw projection data. To solve this, one may want to combine the proposed method with a material decomposition from inconsistent rays (MDIR) algorithm⁵¹ which employs an iterative polychromatic forward projection mechanism. It has to be noted that except the available commercial DECT configurations, triple-energy measurements could also be acquired by a multi-source CT geometry which was originally proposed for ultrafast CT imaging⁵².

In this study, we have used the multi-variable downhill simplex numerical optimization algorithm to solve (4). Note that this is a typical least square problem and other optimization algorithms can be applied to solve the problem, such as Levenberg-Marquardt algorithm. For multi-material decomposition, volume conservation²⁶ and mass conservation²⁵

can be used to regularize the least-square problem, which may be helpful for the optimization procedure. Image domain material decomposition methods are widely used in routine application today. In essence, these methods are based on linear combinations of the reconstructed high- and low-energy CT images. As a comparison, the proposed method provides a nonlinear way to obtain material- and energy-selective images, hence, it may outperform the routinely used linear image-domain methods on contrast-to-noise ratio (CNR) and artifacts reduction¹⁹. Since material decomposition is usually an ill-posed inverse problem, noise is magnified in this procedure, which introduces streaks in the reconstructed material images. Future study will focus on mitigating the streaks by introducing statistical iterative reconstruction and regularized reconstruction^{8,13,14}.

In (3), projection estimation based on the integrals of the material-selective images does not take scatter radiation into account. Hence, the presence of scatter radiation may influence the decomposition procedure, yielding inaccurate line integrals and further inaccurate material-selective images. During the numerical evaluation, scatter radiation is not considered. For realistic applications, one may want to perform scatter correction in front of the material decomposition. To perform scatter correction, the scatter radiation needs to be estimated and then subtracted from the raw projection data⁵³⁻⁵⁶. This would be performed for both dual- and triple-energy measurements.

VI. CONCLUSION

A nonlinear material decomposition framework for both dual- and triple-energy CT is developed and its feasibility of quantitative material decomposition with estimated spectra is demonstrated using scanning protocols for clinically realistic applications. With energy-integrating detector-based DECT configurations, the method shows robustness against spectrum estimation and can provide material-specific images that are comparable to photon-counting CT. It is promising that many CT-based diagnostic and therapy applications will greatly benefit from the proposed material decomposition technique.

VII. APPENDIX

The optimization strategy used in this study is Nelder-Mead method which is a numerical method to find the minimum of (4) in a multidimensional space. For two-variable case (DECT), the method initializes with three randomized vertices in the parameters space (note that each vertex has two components). These three vertices form

a triangle. The algorithm then compares function values at the three vertices (the best \mathbf{B} , the good \mathbf{G} , and the worst \mathbf{W}) of the triangle, i.e., $f(\mathbf{B}) < f(\mathbf{G}) < f(\mathbf{W})$. The worst vertex, where the objective function value is maximum, is rejected and replaced with a new vertex. The operations to generate a new vertex include: reflect, extend, contract and shrink. All of the operations are based on the current triangle. With the new vertex, a new triangle is formed, and the search is continued. The process generates a sequence of triangles, for which the function values at their corresponding vertices get smaller and smaller, until the minimum vertex (the optimal A_i) are found. The algorithm used to solve (4) can be summarized as follows:

Algorithm

1. Initialize $A_i^{(0)}$;
2. Randomly initialize three points (DECT) in the parameter space for the first triangle: $A_i^{(0)}[k]$, $k = 1, 2, 3$;
3. Calculate objective function values: $f(A_i[k]) \leftarrow A_i^{(0)}[k]$;
4. Ranking: $f(\mathbf{B}) < f(\mathbf{G}) < f(\mathbf{W}) \leftarrow f(A_i[k])$;
5. Calculate the reflect point $f(\mathbf{R})$;
6. **WHILE** (criterion is satisfied){
7. **IF**($f(\mathbf{R}) < f(\mathbf{G})$){
8. **IF**($f(\mathbf{B}) < f(\mathbf{R})$)
9. replace \mathbf{W} with \mathbf{R}
10. **ELSE**{
11. compute extend point \mathbf{E} and $f(\mathbf{E})$
12. **IF**($f(\mathbf{E}) < f(\mathbf{B})$)
13. replace \mathbf{W} with \mathbf{E}
14. **ELSE**
15. replace \mathbf{W} with \mathbf{R} }
16. }
17. **ELSE**{
18. **IF**($f(\mathbf{R}) < f(\mathbf{W})$)
19. replace \mathbf{W} with \mathbf{R}
20. compute center point \mathbf{C} and $f(\mathbf{C})$
21. **IF**($f(\mathbf{C}) < f(\mathbf{W})$)

```

22.     replace  $\mathbf{W}$  with  $\mathbf{C}$ 
23. ELSE{
24.     compute shrink point  $\mathbf{S}$  and  $f(\mathbf{S})$ 
25.     replace  $\mathbf{W}$  with  $\mathbf{S}$ 
26.     replace  $\mathbf{G}$  with  $\mathbf{M}$ } //  $\mathbf{M}$  is the midpoint of the good size, i.e.,  $\mathbf{M} = (\mathbf{B} + \mathbf{G})/2$ 
27. }
28.}

```

In this work, we have initialized $A_i^{(0)}[k] = 0$ for all of studies. The **WHILE** loop is stopped when either the maximum iteration 200 is satisfied or the difference between $A_i^{(k-1)}$ and $A_i^{(k)}$ is smaller than 10^{-6} . It takes about 4600 seconds to decomposition DECT sinograms (1024×720) using a typical PC (Intel Core i7-6700K, RAM 32GB).

ACKNOWLEDGMENT

This work was partially supported by NIH (7R01HL111141, 1R01 CA176553 and R01E0116777). The contents of this article are solely the responsibility of the authors and do not necessarily represent the official NIH views. This work was also supported by the Natural Science Foundation of China under Grant No. 61601190. The authors are grateful to our colleague Kai Cheng for proofreading the manuscript.

a) lei@stanford.edu, jkm2001@med.cornell.edu

¹Alvarez RE, Macovski A. Energy-selective reconstructions in x-ray computerised tomography. *Phys Med Biol.* 1976; 21(5):733-744.

²Johnson TR, Krauss B, Sedlmair M, et al. Material differentiation by dual energy CT: initial experience. *Eur Radiol.* 2007; 17(6):1510-1517.

³McCollough CH, Leng S, Yu L, Fletcher JG. Dual-and multi-energy CT: principles, technical approaches, and clinical applications. *Radiology.* 2015;276(3):637-653.

⁴Kalender WA, Perman W, Vetter J, Klotz E. Evaluation of a prototype dual-energy computed tomographic apparatus. I. phantom studies. *Med Phys.* 1986;13(3): 334-339.

⁵Silva AC, Morse BG, Hara AK, Paden RG, Hongo N, Pavlicek W. Dual-energy (spectral) CT: applications in abdominal imaging. *Radiographics.* 2011;31(4): 1031-1046.

⁶Carmi R, Naveh G, Altman A. Material separation with dual-layer CT. in *Nuclear Science Symposium Conference Record, IEEE.* 2005;4: 3.

⁷Yan CH, Whalen RT, Beaupre GS, Yen SY, Napel S. Reconstruction algorithm for polychromatic CT imaging: application to beam hardening correction. *IEEE Trans Med Imaging.* 2000; 19(1): 1-11.

- ⁸O'Sullivan JA, Benac J, Williamson JF. Alternating minimization algorithm for dual energy X-ray CT. in *Proc. IEEE International Symposium on Biomedical Imaging*. 2004; 579-582.
- ⁹Sidky EY, Zou Y, Pan X. Impact of polychromatic x-ray sources on helical, cone-beam computed tomography and dual-energy methods. *Phys Med Biol*. 2004; 49(11): 2293-2303.
- ¹⁰Stenner P, Berkus T, Kachelrieß M. Empirical dual energy calibration (EDEC) for cone-beam computed tomography. *Med Phys*. 2007; 34(9): 3630-3641.
- ¹¹Noh J, Fessler J, Kinahan PE. Statistical sinogram restoration in dual-energy CT for pet attenuation correction. *IEEE Trans Med Imaging*. 2009; 28(11): 1688-1702.
- ¹²Brendel B, Roessl E, Schlomka JP, Proksa R. Empirical projection-based basis-component decomposition method. in *SPIE Medical Imaging*. 2009; 7258: 72583Y. doi:10.1117/12.811006.
- ¹³Chen Y, O'Sullivan JA, Politte DG, Evans JD, Han D, Whiting BR, Williamson JF. Line integral alternating minimization algorithm for dual-energy x-ray CT image reconstruction. *IEEE Trans Med Imaging*. 2016; 35(2): 685-698.
- ¹⁴Ducros N, Abascal JFPJ, Sixou B, Rit S, Peyrin F. Regularization of nonlinear decomposition of spectral x-ray projection images. *Med Phys*. 2017; 44(9): e174-e187.
- ¹⁵Hohweiller T, Ducros N, Peyrin F, Sixou B. Spectral ct material decomposition in the presence of poisson noise: A kullback-leibler approach. *IRBM*. 2017; 38(4): 214-218.
- ¹⁶Pham MQ, Ducros N, Nicolas B. A BVMF-b algorithm for nonconvex nonlinear regularized decomposition of spectral x-ray projection images. *SPIE Medical Imaging*. 2017; 10132: 101323K.
- ¹⁷Niu T, Dong X, Petrongolo M, Zhu L. Iterative image-domain decomposition for dual-energy CT. *Med Phys*. 2014; 41(4): 041901.
- ¹⁸Clark DP, Badea CT. Spectral diffusion: an algorithm for robust material decomposition of spectral CT data. *Phys Med Biol*. 2014; 59(21): 6445-6466.
- ¹⁹Kuchenbecker S, Faby S, Sawall S, Lell M, Kachelrieß M. Dual energy CT: how well can pseudo-monochromatic imaging reduce metal artifacts? *Med Phys*. 2015; 42(2): 1023-1036.
- ²⁰Sukovic P, Clinthorne NH. Penalized weighted least-squares image reconstruction for dual energy x-ray transmission tomography. *IEEE Trans Med Imaging*. 2000; 19(11): 1075-1081.
- ²¹Zhang R, Thibault JB, Bouman C, Sauer KD, Hsieh J. Model-based iterative reconstruction for dual-energy x-ray CT using a joint quadratic likelihood model. *IEEE Trans Med Imaging*. 2014; 33(1): 117-134.
- ²²Long Y, Fessler J. Multi-material decomposition using statistical image reconstruction for spectral CT. *IEEE Trans Med Imaging*. 2014; 33(8): 1614-1626.
- ²³Barber RF, Sidky EY, Schmidt TG, Pan X. An algorithm for constrained one-step inversion of spectral CT data. *Phys Med Biol*. 2016; 61(10):3784-3818.
- ²⁴Tran DN, Straka M, Roos JE, Napel S, Fleischmann D. Dual-energy CT discrimination of iodine and calcium: experimental results and implications for lower extremity CT angiography. *Academic Radiology*. 2009; 16(2): 160-171.
- ²⁵Liu X, Yu L, Primak AN, McCollough CH. Quantitative imaging of element composition and mass fraction using dual-energy CT: three-material decomposition. *Med Phys*. 2009; 36(5): 1602-1609.
- ²⁶Mendonça PR, Lamb P, Sahani DV. A flexible method for multi-material decomposition of dual-energy CT images. *IEEE Trans Med Imaging*. 2014; 33(1): 99-116.

- ²⁷Xue Y, Ruan R, Hu X, et al. Statistical image-domain multi-material decomposition for dual-energy CT. *Med Phys.* 2017;44(3):886-901.
- ²⁸Roessl E, Proksa R. K-edge imaging in x-ray computed tomography using multi-bin photon counting detectors. *Phys Med Biol.* 2007; 52(15): 4679-4696.
- ²⁹Bornefalk H, Danielsson M. Photon-counting spectral computed tomography using silicon strip detectors: a feasibility study. *Phys Med Biol.* 2010; 55(7): 1999, 2010-2022.
- ³⁰Modgil D, Rigie DS, Wang Y, Xiao X, Vargas PA, La Rivière PJ. Material identification in x-ray microscopy and micro CT using multi-layer, multi-color scintillation detectors. *Phys Med Biol.* 2015;60(20): 8025-8045.
- ³¹Zimmerman KC, Schmidt TG. Experimental comparison of empirical material decomposition methods for spectral CT. *Phys Med Biol.* 2015; 60(8): 3175-3191.
- ³²Zhang Y, Mou X, Wang G, Yu H. Tensor-based dictionary learning for spectral CT reconstruction. *IEEE Trans Med Imaging.* 2017;36(1):142-154.
- ³³Lee O, Kappler S, Polster C, Taguchi K. Estimation of basis line-integrals in a spectral distortion-modeled photon counting detector using low-order polynomial approximation of x-ray transmittance. *IEEE Trans Med Imaging.* 2016;36(2):560-573.
- ³⁴Granton P, Pollmann S, Ford N, Drangova M, Holdsworth D. Implementation of dual-and triple-energy cone-beam micro-CT for postreconstruction material decomposition. *Med Phys.* 2008; 35(11):5030-5042.
- ³⁵Yu L, Li Z, Leng S, McCollough CH. Dual-source multi-energy CT with triple or quadruple x-ray beams. *SPIE Medical Imaging.* 2016;978: 978312.
- ³⁶Punnoose J, Xu J, Sisniega A, Zbijewski W, Siewerdsen J. Technical note: Spektr 3.0: A computational tool for x-ray spectrum modeling and analysis. *Med Phys.* 2016; 43(8): 4711-4717.
- ³⁷Zhao W, Niu K, Schafer S, Royalty K. An indirect transmission measurement-based spectrum estimation method for computed tomography. *Phys Med Biol.* 2015; 60(1): 339-357.
- ³⁸Duisterwinkel H, van Abbema J, van Goethem M, et al. Spectra of clinical ct scanners using a portable compton spectrometer. *Med Phys.* 2015; 42(4): 1884-1894.
- ³⁹Chang S, Mou X. A statistical iterative reconstruction framework for dual energy computed tomography without knowing tube spectrum. *Developments in X-Ray Tomography X.* 2016; 9967: 99671L.
- ⁴⁰Leinweber C, Maier J, Kachelrieß M. X-ray spectrum estimation for accurate attenuation simulation. *Medical Physics,* 2017.
- ⁴¹Zhao W, Xing L, Zhang Q, Xie Q, Niu T. Segmentation-free x-ray energy spectrum estimation for computed tomography using dual-energy material decomposition. *Journal of Medical Imaging.* 2017; 4(2): 023506.
- ⁴²Whiting BR, Massoumzadeh P, Earl OA, O'Sullivan JA, Snyder DL, Williamson JF. Properties of preprocessed sinogram data in x-ray computed tomography. *Med Phys.* 2006; 33(9): 3290-3303.
- ⁴³Wang J, Chai A, Xing L. Noise correlation in cbct projection data and its application for noise reduction in low-dose CBCT. *Proceedings of the SPIE.* 2009; 7258: 72582D.
- ⁴⁴Zhang H, Ouyang L, Ma J, Huang J, Chen W, Wang J. Noise correlation in cbct projection data and its application for noise reduction in low-dose cbct. *Med Phys.* 2014; 41(3): 031906.
- ⁴⁵Prax G, Xing L. GPU computing in medical physics: A review. *Med Phys.* 2011; 38(5): 2685-2697.
- ⁴⁶Cormode DP, Roessl E, Thran A, et al. Atherosclerotic plaque composition: analysis with multicolor CT and targeted gold nanoparticles. *Radiology.* 2010; 256(3): 774-782.

- ⁴⁷Muenzel D, Bar-Ness D, Roessl E, et al. Spectral photon-counting CT: Initial experience with dual-contrast agent K-edge colonography. *Radiology*. 2016; 283(3): 723-728.
- ⁴⁸Atak H, Shikhaliev PM. Dual energy CT with photon counting and dual source systems: comparative evaluation. *Phys Med Biol*. 2015; 60(23): 8949-8975.
- ⁴⁹Yu Z, Leng S, Jorgensen SM, et al. Evaluation of conventional imaging performance in a research whole-body CT system with a photon-counting detector array. *Phys Med Biol*. 2016; 61(4): 1572-1595.
- ⁵⁰Touch M, Clark DP, Barber W, Badea CT. A neural network-based method for spectral distortion correction in photon counting x-ray CT. *Phys Med Biol*. 2016; 61(16): 6132-6153.
- ⁵¹Maaß C, Meyer E, Kachelrieß M. Exact dual energy material decomposition from inconsistent rays (MDIR). *Med Phys*. 2011; 38(2): 691-700.
- ⁵²Neculaes VB, Edic PM, Frontera M, Caiafa A, Wang G, De Man B. Multisource x-ray and CT: Lessons learned and future outlook. *IEEE Access*. 2014;2: 1568-1585.
- ⁵³Zhu L, Xie Y, Wang J, Xing L. Scatter correction for cone-beam CT in radiation therapy. *Med Phys*. 2009; 36(6): 2258-2268.
- ⁵⁴Zhao W, Brunner S, Niu K, Schafer S, Royalty K, Chen G. Patient-specific scatter correction for flat-panel detector-based cone-beam CT imaging. *Phys Med Biol*. 2015; 60(3): 1339-1365.
- ⁵⁵Zhao W, Vernekohl D, Zhu J, Wang L, Xing L. A model-based scatter artifacts correction for cone beam CT. *Med Phys*. 2016; 43(4):1736-1753.
- ⁵⁶Shi L, Vedantham S, Karellas A, Zhu L. X-ray scatter correction for dedicated cone beam breast CT using a forward projection model. *Med Phys*. 2017; 44(6): 2312-2320.